Earth and Planetary Science Letters 484 (2018) 253–263

Contents lists available at ScienceDirect

Earth and Planetary Science Letters

www.elsevier.com/locate/epsl

Changes of deep Pacific overturning circulation and carbonate chemistry during middle Miocene East Antarctic ice sheet expansion

Xiaolin Ma [a,b,*], Jun Tian [a,*], Wentao Ma [a,c], Ke Li [a], Jimin Yu [a,d]

[a] State Key Laboratory of Marine Geology, Tongji University, Shanghai, 200092, China
[b] State Key Laboratory of Loess and Quaternary Geology, Institute of Earth Environment, Chinese Academy of Sciences, Xi'an, 710075, China
[c] State Key Laboratory of Satellite Ocean Environment Dynamics, Second Institute of Oceanography, SOA, Hangzhou 310012, China
[d] Research School of Earth Sciences, the Australian National University, Canberra, ACT 2601, Australia

ARTICLE INFO

Article history:
Received 18 June 2017
Received in revised form 25 November 2017
Accepted 1 December 2017
Available online 28 December 2017
Editor: M. Frank

Keywords:
deep Pacific Ocean circulation
middle Miocene
carbonate chemistry
East Antarctic ice sheet expansion

ABSTRACT

East Antarctic ice sheet expansion (EAIE) at ~13.9 Ma in the middle Miocene represents a major climatic event during the long-term Cenozoic cooling, but ocean circulation and carbon cycle changes during this event remain unclear. Here, we present new fish teeth isotope (εNd) and benthic foraminiferal B/Ca records from the South China Sea (SCS), newly integrated meridional Pacific benthic foraminiferal $\delta^{18}O$ and $\delta^{13}C$ records and simulated results from a biogeochemical box model to explore the responses of deep Pacific Ocean circulation and carbon cycle across EAIE. The εNd and meridional benthic $\delta^{13}C$ records reveal a more isolated Pacific Deep Water (PDW) and a sluggish Pacific meridional overturning circulation during the post-EAIE with respect to the pre-EAIE owing to weakened southern-sourced deep water formation. The deep-water [CO_3^{2-}] and calcium carbonate mass accumulation rate in the SCS display markedly similar increases followed by recoveries to the pre-EAIE level during EAIE, which were probably caused by a shelf–basin shift of $CaCO_3$ deposition and strengthened weathering due to a sea level fall within EAIE. The model results show that the ~1‰ positive $\delta^{13}C$ excursion during EAIE could be attributed to increased weathering of high-$\delta^{13}C$ shelf carbonates and a terrestrial carbon reservoir expansion. The drawdown of atmospheric CO_2 over the middle Miocene were probably caused by combined effects of increased shelf carbonate weathering, expanded land biosphere carbon storage and a sluggish deep Pacific meridional overturning circulation.

1. Introduction

Earth's climate underwent dramatic cooling during the middle Miocene climate transition (MMCT) around 14.2–13.8 Ma, manifested by a 6–7 °C sea surface temperatures (SST) drop in the high-latitude southwest Pacific Ocean (Shevenell et al., 2004). At ~13.9 Ma, a ~1.0‰ increase in benthic foraminiferal $\delta^{18}O$ suggests a large ice sheet expansion in East Antarctic (e.g., Tian et al., 2013), equivalent to ~40–60 m sea level drop (John et al., 2004). During this so-called East Antarctic Ice-sheet Expansion (EAIE), the ocean carbon reservoir also showed a prominent perturbation, characterized by large positive excursions in benthic and planktonic foraminiferal $\delta^{13}C$ in the Pacific Ocean (e.g., Woodruff and Savin, 1991; Holbourn et al., 2005; Tian et al., 2014). These positive excursions are known as Carbon-isotope Maxima (CM) (Vincent and Berger, 1985; Woodruff and Savin, 1991). In total, six CM events, numbered from CM1 to CM6 and paced by 400-kyr eccentricity cycles, have been identified (e.g., Holbourn et al., 2013; Shevenell et al., 2004; Shevenell and Kennett, 2004; Tian et al., 2013, 2014; Woodruff and Savin, 1991). CM6 event is the largest carbon isotope shift, showing a prominent ~1.0‰ increase in benthic foraminiferal $\delta^{13}C$ during ~13.9–13.8 Ma.

Explanations for the causal relationship between deep ocean circulation, EAIE and CM6 mainly fall into two categories. One hypothesis (so-called "CO_2 hypothesis") suggests that EAIE was triggered by an atmospheric pCO_2 drop which was driven by oceanic carbon reservoir changes including variations in carbonate chemistry, organic carbon production, and remineralization (Diester-Haass et al., 2009; Kürschner et al., 2008; Raymo and Ruddiman, 1992; Vincent and Berger, 1985). Existing atmospheric pCO_2 reconstructions have much lower time resolutions than benthic $\delta^{18}O$ records, and different proxies show contradictive results during the middle Miocene (Beerling and Royer, 2011; Foster et al., 2012). It is yet difficulty to verify the "CO_2 hypothesis",

* Corresponding authors at: State Key Laboratory of Marine Geology, Tongji University, Shanghai, 200092, China.
E-mail addresses: 86_PaleoMa@tongji.edu.cn (X. Ma), tianjun@tongji.edu.cn (J. Tian).

https://doi.org/10.1016/j.epsl.2017.12.002
0012-821X/

given the poor timing control of atmospheric pCO_2 relative to the ice sheet growth in Antarctic. The other hypothesis ("ocean circulation hypothesis") states that poleward heat/moisture flux changes, driven by ocean circulation reorganization, were responsible for the ice sheet buildup and global cooling during the middle Miocene (e.g., Holbourn et al., 2005, 2013; Shevenell et al., 2004; Tian et al., 2009; Woodruff and Savin, 1991). Holbourn et al. (2013) suggested that following EAIE intermediate and deep water productions in the Southern Ocean strengthened the meridional overturning circulation and ventilation of the deep Pacific. However, this deep circulation pattern failed to explain the absence of CM6 event registered in the deep western Pacific Ocean (Tian et al., 2009). At present, deep Pacific Ocean circulation regime, carbonate chemistry changes and atmospheric pCO_2 are poorly constrained and their climatic roles remain unclear during MMCT.

To better understand the link between deep Pacific Ocean circulation, carbon cycle and EAIE during the middle Miocene, the middle Miocene requires high-quality paleoceanographic records based on well-calibrated proxies from multiple sites in the Pacific Ocean. In this study, we present new neodymium isotopic (εNd) records using fossil fish teeth, carbonate ion concentrations ($[CO_3^{2-}]$) derived from benthic foraminiferal boron-to-calcium (B/Ca) ratios, and carbonate accumulation rates from the western Pacific Ocean during MMCT. Combined with published benthic foraminiferal $\delta^{13}C$ records, we investigate the deep Pacific Ocean circulation changes and their links to Antarctic ice sheet expansion and carbon cycle during this transition. Finally, we use a biogeochemical box model to diagnose mechanisms causing the carbon cycle perturbation associated with EAIE.

2. Modern deep Pacific Ocean circulation

Today, the intermediate Pacific Ocean is occupied by two fresh, low-salinity water masses, the Antarctic Intermediate Water (AAIW) and the North Pacific Intermediate Water (NPIW) (Figs. 1b and c). AAIW is ventilated in the Southern Ocean and traceable throughout the South Pacific. By contrast, NPIW is confined to the subtropical North Pacific and ventilated in the Okhotsk Sea (Talley et al., 2011), where Dense Shelf Water is produced in coastal polynyas by brine rejection during winter sea-ice production. No deep water is formed in the modern subarctic Pacific, as surface waters are isolated from subsurface waters by a steep halocline, which leads to a robust surface ocean stratification in this region (Fig. 1c). AAIW spreads northward at ~500–1500 m water depth to ~10°S where it mixes with NPIW from the north.

In the South Pacific Ocean, water masses underlying AAIW include high-salinity Circumpolar Deep Water (CDW) and Antarctic Bottom Water (AABW) (Figs. 1b and c). Densest AABW is usually confined south of 50°S in the abyssal ocean. Depending on their densities, CDW can be further divided into Upper Circumpolar Deep Water (UCDW) and Lower Circumpolar Deep Water (LCDW), which flow northward into the central Pacific Ocean Basin (Figs. 1a and b). The southern-sourced deep waters are diffusively transformed into Pacific Deep Water (PDW), with little contribution of surface waters from the North Pacific (Figs. 1a and b). Hence, PDW represents an aged water mass characterized by low dissolved oxygen, high nutrients and negative $\delta^{13}C$ compared to relatively younger water masses formed in the Southern Ocean (Fig. 1b). The southward PDW return flow contributes to UCDW at 2000–3000 m depth in the South Pacific (Figs. 1a and b).

3. Materials and methods

3.1. ODP Site 1148

Ocean Drilling Program (ODP) Site 1148 (18°50.169′N, 116°33.939′E; 3294 m water depth) is located at the lower continental slope of the northern South China Sea (SCS) (Fig. 1a). During Quaternary, the deep SCS is connected to the open Pacific Ocean via Luzon Strait with the deepest sill depth of 2650 m, below which deep SCS waters are well mixed showing similar physicochemical characteristics as deep waters in the open Pacific Ocean (Qu et al., 2006). The tectonic history of the SCS was closely related to India-Eurasia continental collision and the subduction of the Pacific Plate. The previous researches suggested the age of the SCS is from ~32 Ma to 17 or 16 Ma (Taylor and Hayes, 1980, 1983; Briais et al., 1993; Seton et al., 2012). This result is further supported by the recently acquired deep tow magnetic anomalies and International Ocean Discovery Program (IODP) Expedition 349 cores, which indicated the onset of seafloor of SCS occurred between 32–31.5 Ma and seafloor spreading was terminated at ~15 Ma (Li et al., 2014). Then, the SCS oceanic crust was subducted eastward beneath the West Philippine Sea Plate along the Manila Trench, which produced an accretion prism and a volcanic arc between Taiwan and Luzon Islands (Huang et al., 1997; Queano et al., 2007). At around 10 Ma, the Palawan and the Borneo/Kalimantan were subducted beneath the double subduction zone between the SCS oceanic crust and the Philippine plate, which established the semi-closed SCS formation and likely caused significant uplift of the central sill of between the Taiwan and Luzon in the Late Miocene (Queano et al., 2007; Seton et al., 2012). At least before 10 Ma, the deep SCS was entirely open to the deep west Pacific Ocean, allowing the use of ODP Site 1148 to infer deep Pacific Ocean circulation changes. ODP Site 1148 unfolds an 853-m-thick sediment succession covering the time since the Late Oligocene (Wang et al., 2000). The Middle Miocene lithology mainly contains olive-gray and reddish-brown clays with nanofossils, and show a sedimentation rate of ~15 mm/kyr and carbonate contents of ~40% (Wang et al., 2000). The age model for ODP Site 1148 is readjusted to that of IODP Site U1337 (Tian et al., 2013) by correlating their benthic $\delta^{18}O$ records (Tian et al., 2008).

3.2. Fish teeth εNd

In the ocean, seawater Nd is mainly derived from continental weathering. The interocean contrast of deep water εNd is dominated by the distribution of ancient and juvenile crusts surrounding the ocean. The modern Southern Ocean sourced waters have εNd values ranging from −8 to −9, while εNd of deep North Pacific waters span from −4 to −6 (e.g., Frank, 2002). Neodymium has a short residence time of 300–1000 yrs in the ocean, shorter than the mean oceanic mixing time (e.g., Scher et al., 2015). This renders seawater εNd to be sensitive to ocean circulation and water mass mixing. Deep-water εNd can be recorded by fish teeth apatite, not biased by post-deposition processes (Martin and Scher, 2004). This allows the use of fish teeth εNd to reconstruct ocean circulation changes in the past.

We measured εNd in fossil fish teeth from ODP Site 1148 to investigate Pacific overturning circulation changes during EAIE. For each sample, 2–5 fish teeth debris were picked from the >150-μm size fraction, and checked by scanning electron microscopy. Fish teeth samples were then cleaned by quartz-distilled water and methanol, followed by reductive, oxidative, and weak acid cleaning steps. The cleaned fish teeth were finally dissolved in quartz-distilled 0.25 M HCl. Nd was then purified using the single column method (Scher et al., 2015), with the only change being a doubling column length to improve separation of samarium. εNd were measured on a Neptune multiple collector inductively coupled plasma mass spectrometer (MC-ICP-MS) at the Center for Elemental Mass Spectrometry (University of South Carolina). The mass fractionation was corrected by normalizing $^{146}Nd/^{144}Nd$ to 0.7219 and using exponential-fractionation correction. During analysis, each sample

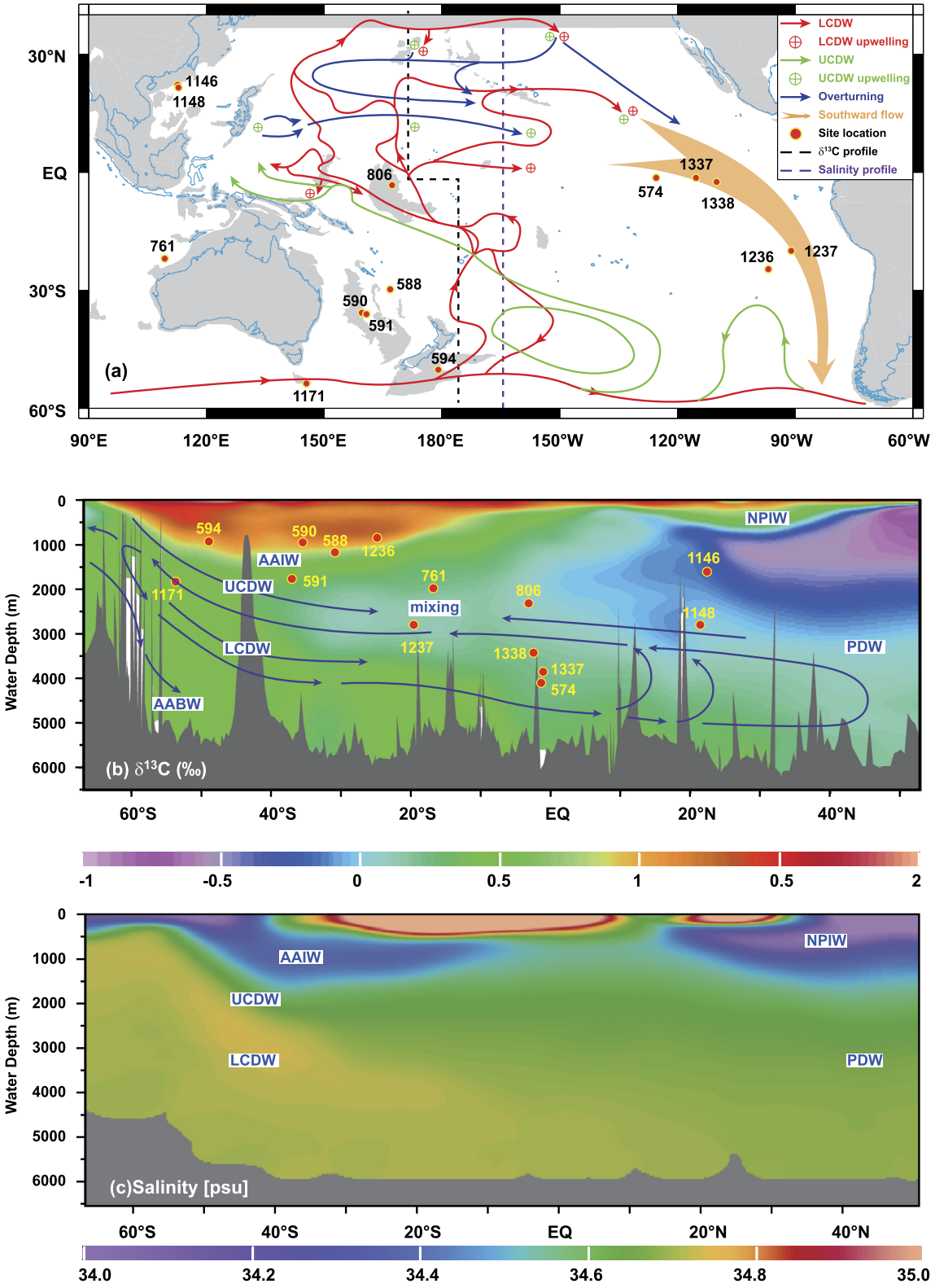

Fig. 1. (a) Paleogeographic reconstructions at 14 Ma showing today's deep Pacific Ocean circulation (revised from Kawabe and Fujio, 2010) and sites used in this study. Paleogeographic reconstructions were generated using the Internet-based tool available from the Ocean Drilling Stratigraphic Network (Hay et al., 1999). Cyan lines represent the modern continents, and gray areas represent the continental plates at 14 Ma. Red lines with arrows represent Lower Circumpolar Deep Water (LCDW). Red circles with a central cross denote the upwelling locations of LCDW. Green circles with a central cross denote LCDW upwelling routes that mix with North Pacific Deep Water (NPDW), and flows are indicated by the blue lines with arrows. Bold orange arrow represents the southward overturning that brings modified NPDW to mix with the Upper Circumpolar Deep Water (UCDW) and then returns it to the Southern Ocean. Green lines with arrows represent spatial distribution of UCDW. (b) A schematic showing deep Pacific overturning circulation, indicated by the blue lines with arrows, in the context of the modern seawater $\delta^{13}C$ profile along the Pacific meridional transect based on the GLODAP dataset (Key et al., 2004) (black dashed line in (a)). (c) Modern seawater salinity profile along the Pacific meridional transect based on WOA13 dataset (purple dashed line in (a)). Red dots with yellow numbers are the study sites in (a) and their projection on the meridional transect (b). AABW = Antarctic Bottom Water, AAIW = Antarctic Intermediate Water. (For interpretation of the references to color in this figure legend, the reader is referred to the web version of this article.)

Table 1
Site locations, water depths, and data sets discussed in this study.

Site	Longitude	Latitude	Paleo-longitude	Paleo-latitude	Water depth (m)	Paleo-water depth (m)	$\delta^{13}C$ 14.1 Ma	$\delta^{13}C$ 13.5 Ma	References
DSDP 574	133.33°W	4.21°N	135.3W	1.4°S	4561	4103	1.8	1.3	Pisias et al., 1985
DSDP 588	161.23°E	26.11°S	157°E	30.8°S	1533	1185	2.1	1.6	Flower and Kennett, 1995
DSDP 590	163.36°E	31.17°S	159.6°E	35.6°S	1299	951	2.3	1.6	Flower and Kennett, 1995
DSDP 591	164.449°E	31.58°S	160.8°E	36.5°S	2131	1783	2.3	1.3	Flower and Kennett, 1995
DSDP 594	174.95°E	45.52°S	178.2°E	48.9°S	1204	922	1.9	1.7	Flower and Kennett, 1995
ODP 761	115.54°E	16.74°S	109.3°E	21.8°S	2189	1988	1.5	1.3	Holbourn et al., 2004
ODP 806	159.36°E	0.32°N	167.3°E	3.3°S	2520	2311	1.9	1.2	Holbourn et al., 2013
ODP 1146	116.27°E	19.45°N	121.6°E	22.3°N	2095	1600	1.3	0.8	Holbourn et al., 2005
ODP 1148	116.57°E	18.83°N	121.9°E	21.6°N	3294	2799	0.8	1.05	Tian et al., 2009; this work
ODP 1171	149.11°E	48.50°S	145.2°E	53.7°S	2148	1833	1.8	1.3	Shevenell et al., 2004, 2008
ODP 1236	81.44°W	21.36°S	96.8°W	24.8°S	1323	833	2.0	1.4	Holbourn et al., 2013
ODP 1237	76.38°W	16.01°S	91°W	19.8°S	3212	2799	1.9	1.4	Holbourn et al., 2005, 2007
IODP U1337	123.2°W	3.83°N	115.2°W	1.2°S	4472	3855	1.6	1.1	Tian et al., 2013
IODP U1338	117.97°W	2.51°N	110°W	2.2°S	4200	3415	1.6	1.1	Holbourn et al., 2014

was bracketed with analyses of Nd standard solutions of JNdi-1. The long term external reproducibility (2σ, $n = 30$) of the Nd isotopes was assessed by repeated measurement of JNdi-1 standard at a concentration similar to that of the sample and yielded 0.25 εNd units. Detailed information about the method is described in Scher et al. (2015).

3.3. Benthic B/Ca

Deep water [CO_3^{2-}] has been used as a useful parameter to reconstruct past seawater carbonate chemistry, which determines calcium carbonate saturation state (Ω) and hence affects deep-sea $CaCO_3$ dissolution/preservation with important implications for mechanisms responsible for the global carbon cycle. We have measured benthic foraminiferal B/Ca to reconstruct deep water [CO_3^{2-}] during EAIE.

About 6–12 *C. wuellerstorfi* or *C. mundulus* shells were picked from the 250–350 μm size fraction for each sample from ODP Site 1148. Foraminiferal shells were cleaned using the "Mg-cleaning" method, which includes clay and silicate removal, oxidative cleaning, and weak acid leaching steps (Barker et al., 2003). Foraminiferal B/Ca were measured on an ICP-MS using the established procedure (Yu et al., 2007). Duplicate analyses show a standard deviation of ~1.9% (1σ) during the measurements of samples presented in this study. Deep water $\Delta[CO_3^{2-}]$ for Miocene were calculated using the approach from Kender et al. (2014), using the core-top B/Ca-$\Delta[CO_3^{2-}]$ relationship and taking account of past seawater B/Ca variations (Yu et al., 2007, 2013). The Miocene sea water B/Ca was estimated to be ~96% of the modern value based on B and Ca isotopes (Kender et al., 2014).

3.4. Literature cores and age models

In addition to new data, we have compiled benthic foraminiferal $\delta^{13}C$ records from 14 Deep Sea Drilling Project (DSDP)/ODP/IODP sites bathed in various water masses based on the paleodepth estimations and paleogeographic reconstructions at 14 Ma (Figs. 1a, b and S1). Paleodepths were estimated for each site in our compilation using backtracking based on the method from Sclater et al. (1985), which takes into account the underlying oceanic crust age and assumes standard subsidence rates over the last 14 Ma. Detailed information about the method is described in Sclater et al. (1985). Basement age and sediment thickness for each site were taken either from DSDP, ODP and IODP site reports or from map data downloaded from ftp://ftp.es.usyd.edu.au/pub/agegrid/2008/Grids (Table S1). Our depth estimates are similar to previous estimates using different methods (Table 1 and Table S1). The palaeogeographic map and site locations at 14 Ma were generated based on the Internet-based tool available from the Ocean Drilling Stratigraphic Network, plate tectonic reconstruction service (Fig. 1a and Table S1) (Hay et al., 1999; http://www.odsn.de/odsn/services/paleomap/adv_map.html).

A uniform age model was developed for these cores during the middle Miocene (Table 1; Figs. 1 and S2). IODP Site U1337 benthic $\delta^{18}O$ was selected as the tuning target, for its robust astronomically tuned age model and high resolution (2–3 kyr) (Fig. S2) (Tian et al., 2013). At this site, globally recognized glaciation (Mi3 and Mi4) and CM events are identifiable from $\delta^{18}O$ and $\delta^{13}C$ records. Five distinctive isotopic events including Mi4b (12.6 Ma), Mi4a (13 Ma), Mi3 (13.65 Ma), middle EAIE (13.86 Ma), and Miocene Thermal Maximum (MTM; 15.55 Ma) were used as age tie points for benthic $\delta^{18}O$ from 9 cores using AnalySeries 2.0.8. The original age models from ODP Site 761, DSDP site 594, DSDP site 591 and DSDP site 590 were used due to the low-resolution benthic $\delta^{18}O$ records; $\delta^{18}O$ at these sites increased at ~13.9 Ma (Fig. S1), suggesting reliable age models. Benthic $\delta^{18}O$ and $\delta^{13}C$ on the uniform age model are presented in Figs. S3a and c, respectively.

Of 14 studied sites (Table 1; Fig. 1), three (DSDP 574 and IODP U1337/U1338; 3.4–3.8 km, paleo-water depth) are bathed in LCDW (Pisias et al., 1985; Tian et al., 2013; Holbourn et al., 2014), four (DSDP 588/590/594 and ODP 1236; 9.2–1.2 km, paleo-water depth) are located close to water depths of AAIW (Holbourn et al., 2013). These two group of cores were used to produce stack $\delta^{13}C$ records for LCDW and AAIW (Fig. 2b), respectively, using Locally Weighted Scatterplot Smooth (LOESS). ODP 1171 (1.8 km, paleo-water depth) is from the depth of UCDW (Shevenell et al., 2004, 2008). The remaining six sites (DSDP 591, ODP 1237/1146/1148/761/806) located at 1.6–2.8 km from 36°S–23°N (paleo latitude) are used to reconstruct deep water mass variations from the North Pacific (Holbourn et al., 2004, 2005, 2013; Tian et al., 2008, and this study).

3.5. Box model

We employed a biogeochemical box model to explore deep Pacific carbonate chemistry responses to various carbon cycle perturbation scenarios during the EAIE. The model used (Ma et al., 2011) contains one atmospheric and six oceanic boxes (Fig. S4a), with physical and biogeochemical schemes detailed in Fig. S4. Briefly, the model has three boxes to represent south (south of 45°S), equatorial (45°S–45°N), and north (north of 45°N) upper (0–200 m) oceans. Two boxes are used to represent deep Southern Ocean (S of 45°S) and the rest deep ocean between 200 m to 2500 m. One box is used to represent the global deep ocean below 2500 m. Deep water flows and water mixing fluxes are defined to reflect ocean circulation. Model biogeochemistry is tracked by vari-

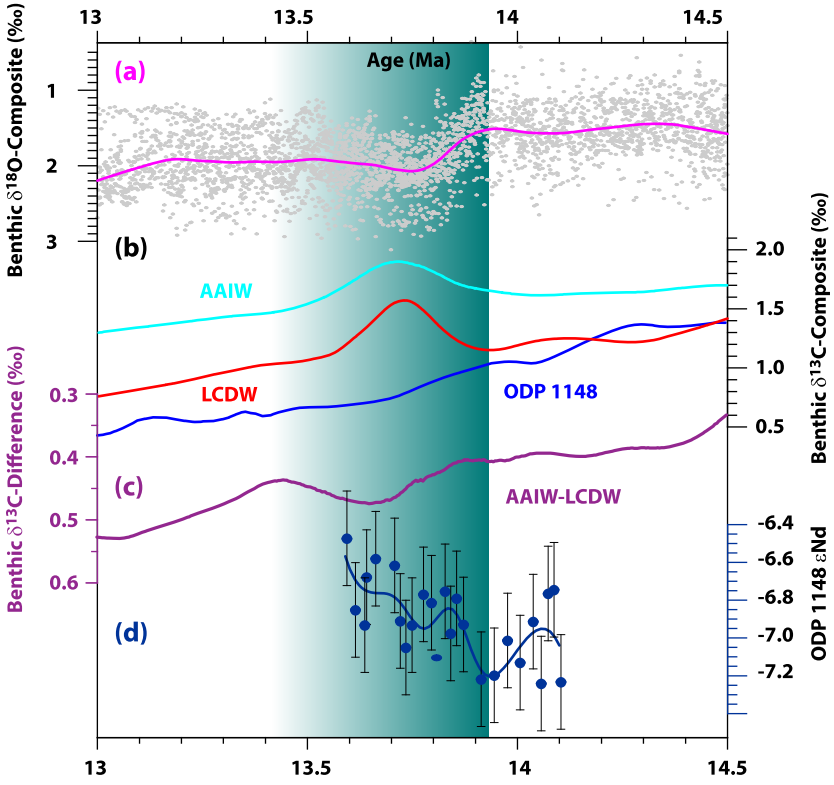

Fig. 2. (a) Stacked benthic $\delta^{18}O$ records from the 14 sites based on a uniform age model. The pink line represents the average benthic $\delta^{18}O$ record trend. (b) Stacked benthic $\delta^{13}C$ records for AAIW (cyan), LCDW (red), and ODP Site 1148 (blue), (c) benthic $\delta^{13}C$ difference between the AAIW and LCDW, (d) fossil fish teeth εNd at ODP Site 1148. The average lines show in (a)–(d) are based on the 0.2-pt LOESS smoothing spline. AAIW = Antarctic Intermediate Water, LCDW = Lower Circumpolar Deep Water.

ables including ALK, atmospheric pCO_2, DIC and $\delta^{13}C$. Carbonate and silicate weathering supplies DIC and ALK to the surface boxes via riverine inputs. Particulate organic carbon (POC) produced by phytoplankton sinks and remineralizes in deep waters with ~0.5% POC eventually preserved in sediments (Ma et al., 2011). $CaCO_3$ burial occurs in both shallow and bottom waters. Atmosphere receives CO_2 degassing from volcanoes and kerogen, and exchanges CO_2 with three surface boxes.

4. Results and discussion

4.1. Benthic $\delta^{13}C$

Spatio-temporal $\delta^{13}C$ variabilities are influenced by multi-factors including isotopic fractionation during air–sea CO_2 exchange, biological processes, and mixing between water masses. Fig. 1b presents meridional $\delta^{13}C$ distributions along a section in the Pacific Ocean, showing southward extension of low-$\delta^{13}C$ PDW at 2–3 km water depth into high-$\delta^{13}C$ AAIW and LCDW. This suggests that, despite biological influences, deep water $\delta^{13}C$ may be used to infer ocean circulation although we caution potential complications associated with this proxy (e.g., Tian et al., 2009; Holbourn et al., 2007, 2013; Shevenell et al., 2004, 2008).

To investigate Pacific overturning circulation changes during EAIE, we reconstructed meridional $\delta^{13}C$ patterns for pre- (~14.1 Ma) and post-EAIE (~13.5 Ma) periods (Fig. 3). Benthic $\delta^{18}O$ and $\delta^{13}C$ records were first smoothed using LOESS to minimize influence from short timescale variabilities (Figs. S3b and d). One prominent feature is that the PDW got more homogeneous from pre- to post-EAIE. We interpret this change to indicate a more isolated PDW and a sluggish Pacific overturning circulation after EAIE. Compared to pre-EAIE, post-EAIE PDW $\delta^{13}C$ became more negative due to a longer residence time that allowed additional decomposition of $\delta^{13}C$-depleted organic matter in the deep North Pacific.

A more sluggish Pacific overturning circulation can also be inferred from $\delta^{13}C$ time series of major water masses. Our stack $\delta^{13}C$ for AAIW and LCDW show that coincident with a benthic $\delta^{18}O$ increase their gradient increased by ~0.2‰ across EAIE (Figs. 2b–c). This $\delta^{13}C$ gradient change was mainly driven by a $\delta^{13}C$ decrease of LCDW, consistent with mixing with aged low-$\delta^{13}C$ PDW. Contrast to our interpretation, Holbourn et al. (2013) attributed the increased $\delta^{13}C$ gradient to greater southward penetration of low-$\delta^{13}C$ PDW and an expansion of high-$\delta^{13}C$ AAIW associated with an enhanced overturning Pacific circulation during EAIE.

The largest benthic $\delta^{13}C$ decline during EAIE is observed at ODP Site 1148, but its responsible reasons remain yet unexplained (Fig. 2b). Tian et al. (2009) argued that the absence of CM6 event (positive $\delta^{13}C$ excursion) at this site was not caused by a sedimentary hiatus or carbonate dissolution. Continuous sedimentation at ODP Site 1148 is supported by the prominent benthic $\delta^{18}O$ increase at ~13.8 Ma as shown by the $\delta^{18}O$ stack (Figs. S3a and b). The lack of ~13.8 Ma $\delta^{13}C$ increase at ODP Site 1148 was unlikely caused by local productivity changes, because nearby ODP Site 1146 from SCS but located at a shallower depth showed a distinct CM6 event (Figs. S3c and d; Tian et al., 2009). No significant difference in organic carbon and opal is observed between ODP Sites 1146 and 1148 (Wang et al., 2000; Wang and Lin, 2004; Wang et al., 2004). We suggest that the strong $\delta^{13}C$ decrease at ODP Site 1148 most likely reflects influences from a low-$\delta^{13}C$ water mass with the most likely candidate to be PDW (Figs. 3b and 4c). This interpretation is more straightforwardly shown by spatial $\delta^{13}C$ distributions between pre- and post-EAIE periods (Fig. 3).

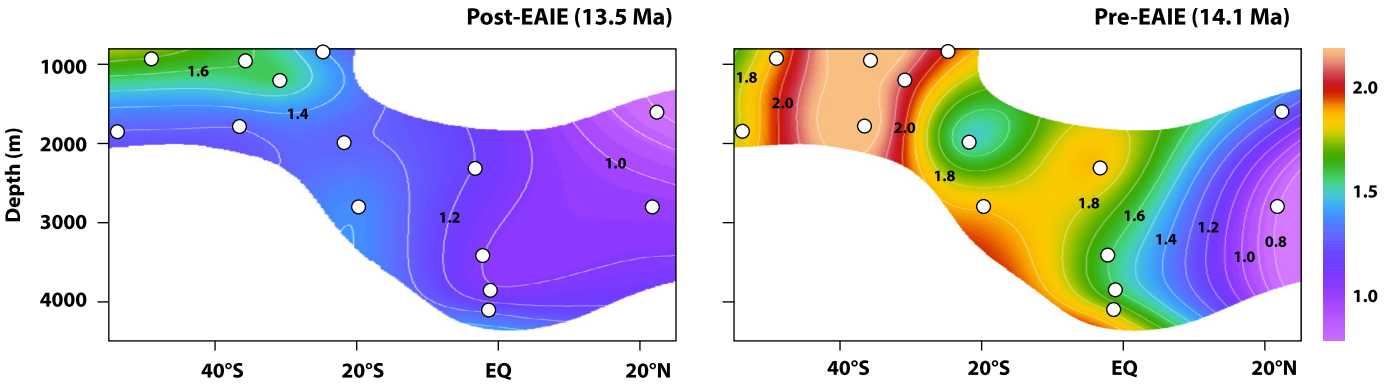

Fig. 3. Pacific meridional distribution of benthic $\delta^{13}C$ for (a) post-EAIE and (b) pre-EAIE, profile (a) and (b) are generated using ODV.

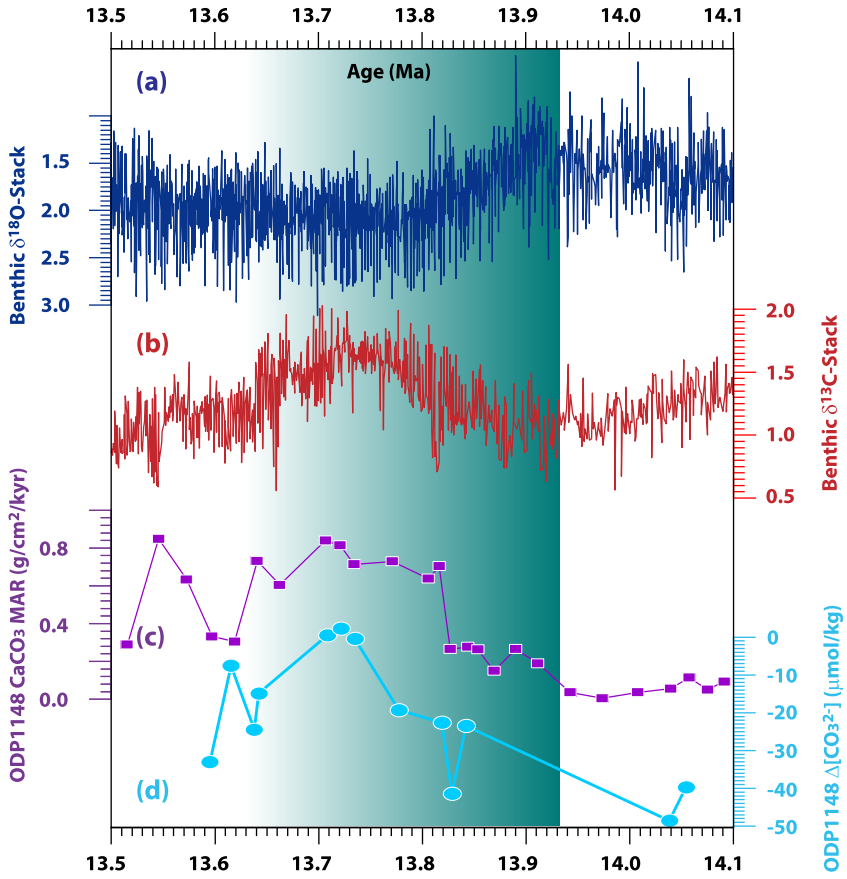

Fig. 4. Stacked (a) benthic $\delta^{18}O$ and (b) $\delta^{13}C$ records for Lower Circumpolar Deep Water. (c) $CaCO_3$ mass accumulation rate (MAR) at ODP Site 1148 (Li et al., 2006), and (d) reconstructed $\Delta[CO_3^{2-}]$ derived from *C. wuellerstorfi* or *C. mundulus* B/Ca ratio at ODP Site 1148.

4.2. Deep Pacific εNd

As mentioned previously, benthic $\delta^{13}C$ is additionally affected by factors such as biology and air–sea exchange that are not directly linked to ocean circulation changes. We therefore use an independent proxy fish teeth εNd to check ocean circulation changes inferred from benthic $\delta^{13}C$. Our high-resolution fish teeth εNd record exhibits an increase from −7.2 to −6.5 at ODP Site 1148 across the EAIE (Fig. 2d). Fish teeth εNd has been widely used to reflect seawater εNd signatures that are mainly influenced by mixing of water masses with different εNd values (e.g. Frank, 2002). Prior to ~13–12 Ma, small inter-basin benthic $\delta^{18}O$ and $\delta^{13}C$ gradients indicate that Southern Ocean was the dominant source of the deep water production with weak North Atlantic Deep Water (NADW) formation through the early–middle Miocene (e.g., Cramer et al., 2009; Woodruff and Savin, 1991). This leaves relatively small influences on Pacific overturning circulation from NADW variations during EAIE. In the Pacific Ocean, middle Miocene north PDW and southern-sourced LCDW had εNd values of ~ −8.5 and ~ −4, respectively (e.g. Holbourn et al., 2013; Frank, 2002). At face value, the εNd increase at ODP Site 1148 would suggest declining proportions of LCDW relative to PDW across EAIE. This water mixing ratio change is consistent with a reduced AABW production around Antarctica, which would be accompanied with a sluggish deep Pacific overturning circulation, a regime inferred from benthic foraminiferal $\delta^{13}C$ (see below). Attention, potential changes in seawater εNd values in the SCS would be affected by the temporal variations in lithogenic Nd input from Asian rivers associated with variations in land-sea configuration and/or East Asian summer monsoon rainfall (Wu et al., 2017). Sea

water εNd records derived from the northern SCS over the last 30 kyr suggest that increase in the lithogenic Nd input associated with the enhanced terrestrial input resulted from the exposed shelf during the LGM would decrease the εNd values (Wu et al., 2017). On the contrary, our εNd records show a more radiogenic trend accompanied by an increased terrestrial input due to the sea level fall and enhanced rainfall linked to the northward shift of the Intertropical Convergence Zone during the EAIE (Tian et al., 2008; Holbourn et al., 2010). This suggests that our εNd variation cannot be attributed to the enhanced terrestrial input.

Recent studies show that radiogenic Nd isotope is added to the deep Pacific from falling particles during water mass advection and aging (Hu et al., 2016; others). The higher εNd might suggest an increased accumulation of more radiogenic Nd during the southward transport of PDW from the North Pacific Ocean to SCS during the post-EAIE period. The accumulation of Nd input from falling particles depends on fluxes of particles and duration of seawater-particle interaction. No significant change is observed in falling particles, based on X-ray fluorescence scanning data from ODP Site 1148 (Tian et al., 2008). Therefore, any increased accumulation of radiogenic Nd associated with PDW would indicate a longer seawater-particle reaction time, which is consistent with a more sluggish Pacific overturning during the post-EAIE period.

4.3. Deep Pacific overturning circulation across EAIE

Deep ocean circulation over geological time might be affected by tectonic events including opening or closure of deep seaways. Nevertheless, no significant large-scale tectonic event occurred in the deep Pacific since the middle Miocene (Hall, 2002). It was suggested that the general deep Pacific Ocean circulation during MMCT was analogous to the modern regime (e.g., Holbourn et al., 2013).

In the middle Miocene, PDW was unlikely sourced from the North Pacific surface waters, as this would raise PDW δ^{13}C, opposite to observation (Fig. 3a). Accordingly, the PDW during MMCT, with a negative δ^{13}C, should have been formed largely by upwelling and diffusion of southern-sourced waters (Fig. 1b). Thus, the deep Pacific circulation over the middle Miocene would largely depend on the variability of the Southern Ocean.

Sea ice expansion and cold water temperature surrounding Antarctica would have an important effect on the deep water formation in the Southern Ocean, thus largely regulating the distribution of deep Pacific water masses. Latest model results suggest that weaker AABW at LGM should lead to a negative δ^{13}C anomalies in the Southern Ocean and Pacific Ocean due to an increase in respired carbon (Menviel et al., 2017), as well as poorly ventilated deep Pacific (e.g., Skinner et al., 2015). Moreover, an equatorward shift of sea ice around Antarctica will generate a shallow isopycnal in the Southern Ocean, and turbulent mixing is no longer able to drive substantial upwelling of PDW across the isopycnal, hence results in a strong stratification and more insolated deep water (Ferrari et al., 2014). EAIE is expected to have resulted in an expansion of the area covered by sea ice, which is supported by the drill core date from the Western Ross Sea (Levy et al., 2016). Therefore, we surmise that the post-EAIE Pacific overturning circulation should be more sluggish, as well as a weaker deep water formation in the Southern Ocean. It is supported by the depleted δ^{13}C in the deep Pacific Ocean (Fig. 2a).

The Southern Ocean played a vital role in regulating the CO_2 storage on glacial–interglacial time scales associated with the biological pump (Sigman et al., 2010). Nitrogen isotope data has been used to argue for more complete nutrient consumption in the Antarctic and more CO_2 storage in the deep ocean during ice ages, probably attributed to the iron fertilization associated with raising dust fluxes (e.g. Sigman et al., 2010; Jaccard et al., 2013). In this process, the ^{13}C-depleted organic carbon sinks out of the surface ocean, and enriches δ^{13}C of the surface waters, as well as releases low δ^{13}C carbon and decreases the δ^{13}C of DIC in the deep ocean due to organic matter degradation and thus a larger $\Delta\delta^{13}$C between surface-intermediate and deep water masses in the Southern Ocean relative to the interglacial ages. Therefore, the activated biological pump during cold period associated with EAIE should be an important reason for the intensified δ^{13}C gradient between AAIW and LCDW since the EAIE (Figs. 2b and c).

As well as the position of mid-latitude westerlies in the Southern Hemisphere plays a critical role in the upwelling and ventilation around Antarctica (e.g. Toggweiler et al., 2006). When the westerlies are aligned with the ACC, they produce a larger divergence and more upwelling of nutrient-rich deep water driven by the northward surface Ekman layer in the Southern Ocean (Sigman et al., 2010). The westerlies in the Southern Ocean today are very strong and draw up a large volume of deep water in around Antarctica where it rather easily refreshes the deep water in the Pacific Ocean. At cold period an equatorward shift in the westerlies weakens the deep water overturning circulation, ventilation and causes more respiration CO_2 to accumulate and increased O_2 consumption in the deep ocean (Toggweiler et al., 2006; Jaccard et al., 2013). It further raises the vertical $\Delta\delta^{13}$C between surface-intermediate and deep water masses in the Southern Ocean relative to the interglacial ages.

Taken together, we surmise that the pre- and post-EAIE scenarios are analogous to the modern and LGM, respectively. Therefore, this increased vertical $\Delta\delta^{13}$C between intermediate and deep water masses probably indicates a more isolated PDW and biological nutrient uptake with the EAIE, hence a sluggish Pacific overturning circulation.

4.4. Response of deep Pacific Ocean carbonate system to EAIE

Deep Pacific Ocean circulation and EAIE over the middle Miocene would inevitably cause deep carbonate chemistry perturbations in the Pacific Ocean, including $[CO_3^{2-}]$ and $CaCO_3$ mass accumulation rate (MAR). The $\Delta[CO_3^{2-}]$ derived from benthic foraminiferal B/Ca (Fig. 4d) at ODP Site 1148 increased by ~40 μmol/kg between ~13.9 Ma and 13.75 Ma, followed by a recovery to pre-excursion levels. This is consistent with the trend of $CaCO_3$ MAR form the same core (Fig. 4c), indicating that the calcite compensation depth (CCD) temporarily deepened. Obviously, the increases in $\Delta[CO_3^{2-}]$ and $CaCO_3$ MAR from ~13.9 Ma to 13.75 Ma are nearly synchronous to the marked increases in both benthic δ^{13}C (Fig. 4b) and δ^{18}O (Fig. 4a), indicating close relationship of the carbonate system with the EAIE. Our results thus reveal absolutely changed carbonate chemistry parameters (i.e. DIC and ALK) during the EAIE. DIC and ALK can be expressed as: $DIC = [CO_2] + [HCO_3^-] + [CO_3^{2-}]$ and $ALK \approx [HCO_3^-] + 2[CO_3^{2-}]$. Approximately, $[CO_3^{2-}] \approx 0.6 \times (ALK - DIC)$ (Yu et al., 2016), thus, changes in oceanic ALK and DIC could modulate the deep ocean $[CO_3^{2-}]$, affecting the Ω. ALK and DIC are removed from seawater at a ratio of 2:1 when $CaCO_3$ precipitates, with a net effect to declining seawater $[CO_3^{2-}]$, and vice versa (e.g., Yu et al., 2014).

The deep sea $[CO_3^{2-}]$ can be modulated by water mass mixing, and ALK input from increased continental weathering. Organic matter sinks from the surface where subsequent decomposition decreases $[CO_3^{2-}]$ in the deep ocean. Today, poorly ventilated PDW has the lowest $[CO_3^{2-}]$, ~50 μmol kg^{-1}, while LCDW, formed in the Southern Ocean, has a relative high $[CO_3^{2-}]$ of ~80 μmol kg^1. This $[CO_3^{2-}]$ gradient along the deep water pathway from the Southern Ocean to the North Pacific reflects gradual accumulation of remineralized organic matter (e.g., Yu et al., 2014). In this case, as expected, the isolated PDW and sluggish Pacific overturning circulation since EAIE should have caused low $[CO_3^{2-}]$ and $CaCO_3$

Table 2
Description of model tests

Test	Description
CNTR	The Lower Circumpolar Deep Water (Q3) flux is set to 12 Sv. The treatment of silicate and carbonate weathering are expressed as $Wsil = fsil * (pCO_2/pCO_2ref)^{\alpha s}$ and $Wcar = fcar * (pCO_2/pCO_2ref)$, respectively, where fsil and fcar are baseline values. pCO_2ref is set to 280 ppm and αs is 0.3. fcar is 5.0×10^{12} mol yr^{-1} and fsil is 5.3×10^{12} mol yr^{-1}. The burial of $CaCO_3$ is treated as a liner damping process. If $[CO_3^{2-}]_B$, the carbonate ion concentration of the box "B", is larger than 85 µmol kg^{-1}, $CaCO_3$ burial occurs. If $[CO_3^{2-}]_B$ is less than 85 µmol kg^{-1}, dissolution happens.
Scenario 1: Q3 × (2/3)	Based on the CNTR, Q3 linearly decreases from 12 Sv to 8 Sv over 100 kyr and then remains at 12 Sv.
Scenario 2: Q3 × (2/3) + (Wcarb + Wsil) × 1.5	The setting is same as Scenario 1 except fcar and fsil are set to 7.5 mol yr^{-1} and 7.95 mol yr^{-1}, respectively, during the first 100 kyr after which they return to the initial level.
Scenario 3: Q3 × 1.5 + (Wcarb + Wsil) × 1.5 + COMRIV × 2	The setting is same as Scenario 2 except the flux of the enriched carbon (^{13}C) is set to double by river input over 100 kyr and then return to the initial level.

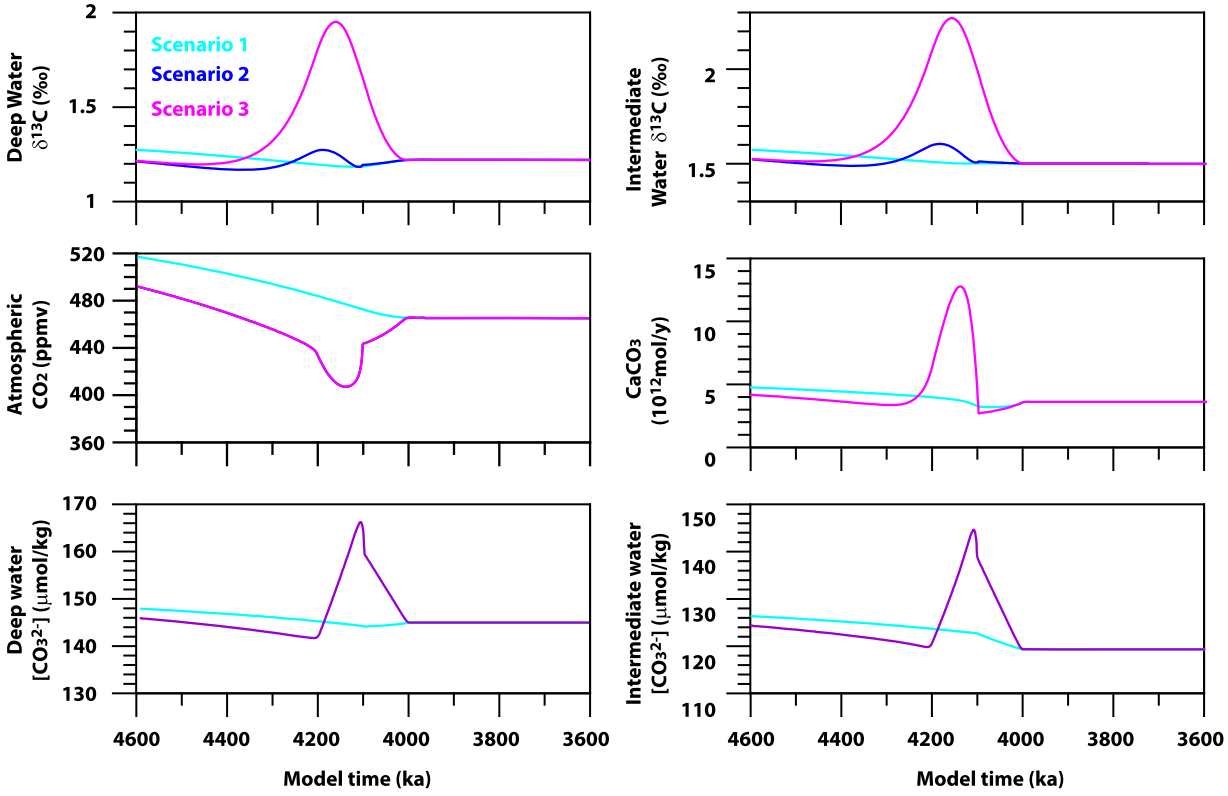

Fig. 5. Simulation results showing evolutions of intermediate and deep water $\delta^{13}C$, atmospheric CO_2, $CaCO_3$ mass accumulation rate (MAR), and intermediate and deep water $[CO_3^{2-}]$ in three scenarios. Please note that Scenario 2 and 3 produce nearly the same results for atmospheric CO_2 and ocean carbonate system.

MAR at ODP Site 1148. Alternatively, increased continental weathering and $CaCO_3$ burial from shallow shelf seas to the deep ocean resulted from sea level fall linked to EAIE were two potential processes that providing extra sources of ALK to the deep ocean.

Further, the high $[CO_3^{2-}]$ and $CaCO_3$ MAR suggest that the isolated PDW and sluggish Pacific overturning circulation should sequestrate more carbon in the deep Pacific Ocean and decrease the atmospheric pCO_2. However, the existing low time resolution atmospheric pCO_2 reconstructions during this time interval cannot verify this deductive decrease.

4.5. Modeling carbon cycle perturbations

We used a biogeochemical box model (Ma et al., 2011) to investigate the carbon cycle perturbation associated with EAIE. The model was tuned to the equilibrium (control run, CNTR) which has an atmospheric concentration of CO_2 (pCO_2) of 464 ppm and a global averaged $\delta^{13}C_{DIC}$ of 1.73‰. The result of CNTR is similar to the state of the Middle Miocene Climate Optimum (MMCO) (Cramer et al., 2009). After reaching a steady state for the control run, we considered three scenarios (Table 2; Fig. 5) that encompass changes with Pacific overturning circulation, weathering and carbon reservoir exchanges (Table 2).

For scenario 1, we tested the effect of Southern Ocean deep water formation changes by decreasing LCDW fluxes linearly from 12 Sv to 8 Sv over 100 kyr, to simulate the sluggish Pacific overturning circulation triggered by EAIE. This simulation produces negligible changes in the calcium carbonate accumulation and $\delta^{13}C$ values in intermediate and deep water masses (Fig. 5), and fails to capture either the ~1‰ positive $\delta^{13}C$ excursion (CM6 event) or the increase in the calcium carbonate accumulation rate (Fig. 5), suggesting that reduced deep water formation and sluggish Pacific overturning circulation is not unique to forcing the carbon cycle perturbation during the EAIE.

In scenario 2, we increased weathering by 50% (including silicate and carbonate) following the above conclusion of increased

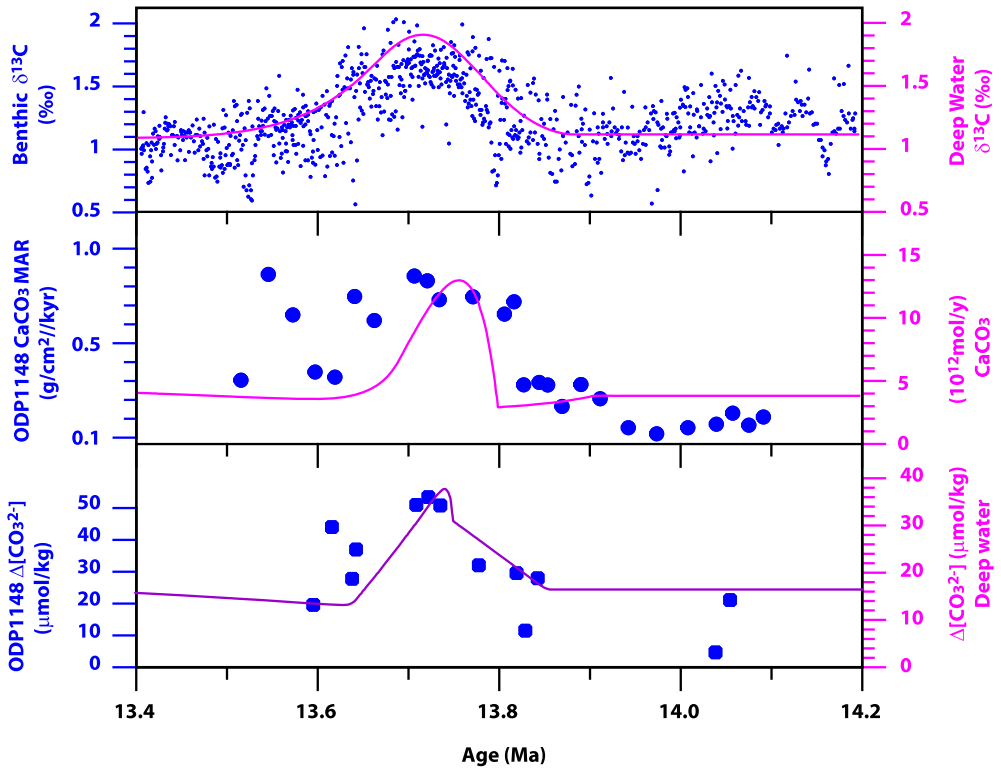

Fig. 6. Comparison between modeled results (pink lines, scenario 3) and paleorecords (blue dots) from 14.2 to 13.4 Ma, indicate the EAIE in the figure. (For interpretation of the references to color in this figure legend, the reader is referred to the web version of this article.)

weathering and/or land C sequestration derived from our deep-water $[CO_3^{2-}]$ record. This scenario produced a significant increase in calcium carbonate accumulation and $[CO_3^{2-}]$ in deep waters (Fig. 5), which is in line with the reconstructed data from ODP Site 1148 and suggests a deepening CCD (Figs. 4c and d). Silicate and carbonate weathering, a sink for atmospheric CO_2, are sources of ALK to the oceans, which potentially provides an explanation for the $CaCO_3$ MAR on sea floor and Antarctic glaciation across the targeted interval of the middle Miocene. A shift from $CaCO_3$ burial in shallow shelf seas to the deep ocean resulted from sea level fall (40–60 m) linked with the EAIE at ~13.8 Ma (John et al., 2004) is coupled with a temporary increase in carbonate weathering from freshly exposed material that could provide a significant ALK supply to the oceans.

In scenario 2, the simulated atmospheric CO_2 rapidly declined by ~70 ppm over 200 kyr (Fig. 5). Unfortunately, there is no high-resolution CO_2 reconstruction from this time interval to test this simulated result. The simulated decline of CO_2 might suggest that increased shelf carbonate weathering associated with Antarctic glaciation were important drivers for CO_2 drawdown during the period of EAIE. However, Scenario 2 produces a very weak increase in $\delta^{13}C$ of only ~0.1‰ in both the deep and intermediate waters, which is much smaller than the observed ~1‰ positive $\delta^{13}C$ excursion in benthic foraminifer (CM6 event; Fig. 4b). Increased weathering could provide more nutrients to the ocean, thus invigorating the biological pump, which transports more ^{12}C from the surface to the deep ocean and counteracts the positive $\delta^{13}C$ excursion. The average $\delta^{13}C$ change in the ocean is mainly affected by the transport of carbon between the ocean, atmosphere and terrestrial reservoirs. Peterson et al. (2014) estimated a global marine $\delta^{13}C$ change for the LGM to the late Holocene of 0.38±0.08‰ for the intermediate and deep oceans, which is roughly equivalent to 400 GtC terrestrial carbon storage change. In addition, sea level fall linked with the growth of the Antarctic ice sheet permanently reduced global $CaCO_3$ MAR on the continental shelves, leading to a rapid weathering of exposed carbonate enriched in ^{13}C, contributing to a positive $\delta^{13}C$ excursion (Armstrong McKay et al., 2016).

Based on scenario 2, scenario 3 considered the variability of the ocean carbon reservoir. Scenario 3 was realized by adding ^{13}C-enriched carbon (2-fold increase) to the ocean through riverine input. Carbon reservoir exchanges have minor impact on the $[CO_3^{2-}]$, $CaCO_3$ and atmospheric CO_2. Therefore, please note that Scenario 2 and 3 produce nearly the same results for atmospheric CO_2 and ocean carbonate system (Fig. 5). The terrestrial vegetation and marine phytoplankton preferentially incorporate ^{12}C rather than ^{13}C into their tissues. If the size of the terrestrial biosphere increases, the light carbon should be sequestered from the ocean–atmosphere system, thus elevating the seawater $\delta^{13}C$. The EAIE at ~13.8 Ma may lead to a northward movement of the Intertropical Convergence Zone (ITCZ) (Holbourn et al., 2010), therefore increasing the moisture transport from the tropical Pacific to the Northern Hemisphere, and further expanding the peatland and vegetation inventories. Moreover, the expansion of permafrost due to Antarctic glaciation could also extract a large amount of carbon from the ocean–atmosphere system (Peterson et al., 2014). Scenario 3 successfully simulated the ~1‰ positive excursion in both the deep and intermediate waters, the high calcium carbonate accumulation rate and the ~40 μmol kg^{-1} increase in deep water $[CO_3^{2-}]$ (Fig. 5), which are in agreement with the reconstructed records from ODP Site 1148 (Fig. 6). The simulated results in this scenario suggest that reduced formation of deep water and a sluggish Pacific overturning circulation together with the shelf carbonate weathering and the sequestration of ^{12}C-enriched carbon account for the carbon cycle perturbation during the EAIE.

5. Conclusion

In this study, we used benthic foraminiferal $\delta^{13}C$, fossil fish teeth εNd, deep-water $[CO_3^{2-}]$ and a biogeochemical box model to explore interactions between ice sheet expansion, deep Pacific

circulation and carbon cycle changes over the period of the East Antarctic Ice Sheet expansion (EAIE). The $\delta^{13}C$ and the fossil fish teeth εNd records indicate a more isolated Pacific Deep Water (PDW) accompanied by a sluggish Pacific overturning circulation during the period of the EAIE which was probably driven by weakened southern-sourced deep water formation at that time. Our modeling results suggest that a shelf-to-basin $CaCO_3$ deposition shift associated with a sea level fall was responsible for the increases in the deep SCS $[CO_3^{2-}]$ and $CaCO_3$ MAR over the EAIE. The $\sim$1‰ positive $\delta^{13}C$ excursion during the CM6 event was attributable to the weathering of $\delta^{13}C$-enriched shelf carbonate and an expansion of $\delta^{13}C$-depleted terrestrial carbon reservoir. Our model results reveal that the increased weathering, more isolated PDW and sluggish Pacific overturning circulation had played important roles in decreasing the atmospheric pCO_2 over the EAIE.

Acknowledgements

We are grateful to the editor and two anonymous reviewers for constructive comments that improve the quality of this paper. This research used samples provided by the Integrated Ocean Drilling Program (IODP). Funding for this research was provided by the NSFC (Grant Nos. 41525020, 91428310, 41676026, 41706071), Shanghai Human Development Fund (201336), and Program of Shanghai Subject Chief Scientist (A type) (16XD1403000). WM thanks the grant of Youth Visiting Ocean-Star Scholars fellowship (QNHX1605) from SOED. JY is also funded by ARC DP140101393 and FT140100993.

Appendix A. Supplementary material

Supplementary material related to this article can be found online at https://doi.org/10.1016/j.epsl.2017.12.002.

References

Armstrong McKay, D.I., Tyrrell, T., Wilson, P.A., 2016. Global carbon cycle perturbation across the Eocene–Oligocene climate transition. Paleoceanography 31, 311–329.

Barker, S., Greaves, M., Elderfield, H., 2003. A study of cleaning procedures used for foraminiferal Mg/Ca paleothermometry. Geochem. Geophys. Geosyst. 4.

Beerling, D.J., Royer, D.L., 2011. Convergent Cenozoic CO_2 history. Nat. Geosci. 4, 418–420.

Briais, A., Patriat, P., Tapponnier, P., 1993. Updated interpretation of magnetic anomalies and seafloor spreading stages in the south China Sea: implications for the Tertiary tectonics of Southeast Asia. J. Geophys. Res., Solid Earth 98, 6299–6328.

Cramer, B., Toggweiler, J., Wright, J., Katz, M., Miller, K., 2009. Ocean overturning since the Late Cretaceous: inferences from a new benthic foraminiferal isotope compilation. Paleoceanography 24.

Diester-Haass, L., Billups, K., Gröcke, D.R., François, L., Lefebvre, V., Emeis, K.C., 2009. Mid-Miocene paleoproductivity in the Atlantic Ocean and implications for the global carbon cycle. Paleoceanography 24.

Ferrari, R., Jansen, M.F., Adkins, J.F., Burke, A., Stewart, A.L., Thompson, A.F., 2014. Antarctic sea ice control on ocean circulation in present and glacial climates. Proc. Natl. Acad. Sci. 111, 8753–8758.

Flower, B.P., Kennett, J.P., 1995. Middle Miocene deepwater paleoceanography in the southwest Pacific: relations with East Antarctic Ice Sheet development. Paleoceanography 10, 1095–1112.

Foster, G.L., Lear, C.H., Rae, J.W., 2012. The evolution of pCO_2, ice volume and climate during the middle Miocene. Earth Planet. Sci. Lett. 341, 243–254.

Frank, M., 2002. Radiogenic isotopes: tracers of past ocean circulation and erosional input. Rev. Geophys. 40, 1-1–1-38.

Hall, R., 2002. Cenozoic geological and plate tectonic evolution of SE Asia and the SW Pacific: computer-based reconstructions, model and animations. J. Asian Earth Sci. 20, 353–431.

Hay, W., et al., 1999. Alternative global Cretaceous paleogeography. In: Barrera, E., Johnson, C. (Eds.), The Evolution of Cretaceous Ocean/Climate Systems. In: Spec. Pap., Geol. Soc. Am., vol. 332, pp. 1–47.

Holbourn, A., Kuhnt, W., Frank, M., Haley, B.A., 2013. Changes in Pacific Ocean circulation following the Miocene onset of permanent Antarctic ice cover. Earth Planet. Sci. Lett. 365, 38–50.

Holbourn, A., Kuhnt, W., Lyle, M., Schneider, L., Romero, O., Andersen, N., 2014. Middle Miocene climate cooling linked to intensification of eastern equatorial Pacific upwelling. Geology 42, 19–22.

Holbourn, A., Kuhnt, W., Regenberg, M., Schulz, M., Mix, A., Andersen, N., 2010. Does Antarctic glaciation force migration of the tropical rain belt? Geology 38, 783–786.

Holbourn, A., Kuhnt, W., Schulz, M., Erlenkeuser, H., 2005. Impacts of orbital forcing and atmospheric carbon dioxide on Miocene ice-sheet expansion. Nature 438, 483–487.

Holbourn, A., Kuhnt, W., Schulz, M., Flores, J.-A., Andersen, N., 2007. Orbitally-paced climate evolution during the middle Miocene "Monterey" carbon-isotope excursion. Earth Planet. Sci. Lett. 261, 534–550.

Holbourn, A., Kuhnt, W., Simo, J.T., Li, Q., 2004. Middle Miocene isotope stratigraphy and paleoceanographic evolution of the northwest and southwest Australian margins (Wombat Plateau and Great Australian Bight). Palaeogeogr. Palaeoclimatol. Palaeoecol. 208, 1–22.

Hu, R., Piotrowski, A.M., Bostock, H.C., Crowhurst, S., Rennie, V., 2016. Variability of neodymium isotopes associated with planktonic foraminifera in the Pacific Ocean during the Holocene and Last Glacial Maximum. Earth Planet. Sci. Lett. 447, 130–138.

Huang, C.-Y., Wu, W.-Y., Chang, C.-P., Tsao, S., Yuan, P.B., Lin, C.-W., Xia, K.-Y., 1997. Tectonic evolution of accretionary prism in the arc-continent collision terrane of Taiwan. Tectonophysics 281, 31–51.

Jaccard, S., Hayes, C.T., Martínez-García, A., Hodell, D., Anderson, R.F., Sigman, D., Haug, G., 2013. Two modes of change in Southern Ocean productivity over the past million years. Science 339, 1419–1423.

John, C.M., Karner, G.D., Mutti, M., 2004. $\delta^{18}O$ and Marion Plateau backstripping: combining two approaches to constrain late middle Miocene eustatic amplitude. Geology 32, 829–832.

Kawabe, M., Fujio, S., 2010. Pacific ocean circulation based on observation. J. Oceanogr. 66, 389–403.

Kender, S., Yu, J., Peck, V.L., 2014. Deep ocean carbonate ion increase during mid Miocene CO_2 decline. Sci. Rep. 4.

Key, R.M., Kozyr, A., Sabine, C.L., Lee, K., Wanninkhof, R., Bullister, J.L., Feely, R.A., Millero, F.J., Mordy, C., Peng, T.H., 2004. A global ocean carbon climatology: results from global data analysis project (GLODAP). Glob. Biogeochem. Cycles 18.

Kürschner, W.M., Kvaček, Z., Dilcher, D.L., 2008. The impact of Miocene atmospheric carbon dioxide fluctuations on climate and the evolution of terrestrial ecosystems. Proc. Natl. Acad. Sci. 105, 449–453.

Levy, R., Harwood, D., Florindo, F., Sangiorgi, F., Tripati, R., von Eynatten, H., Gasson, E., Kuhn, G., Tripati, A., DeConto, R., Fielding, C., Field, B., Golledge, N., McKay, R., Naish, T., Olney, M., Pollard, D., Schouten, S., Talarico, F., Warny, S., Willmott, V., Acton, G., Panter, K., Paulsen, T., Taviani, M., Team, S.S., 2016. Antarctic ice sheet sensitivity to atmospheric CO_2 variations in the early to mid-Miocene. Proc. Natl. Acad. Sci. 113, 3453–3458.

Li, Q., Wang, P., Zhao, Q., Shao, L., Zhong, G., Tian, J., Cheng, X., Jian, Z., Su, X., 2006. A 33 Ma lithostratigraphic record of tectonic and paleoceanographic evolution of the South China Sea. Mar. Geol. 230, 217–235.

Li, C.F., Xu, X., Lin, J., Sun, Z., Zhu, J., Yao, Y., Zhao, X., Liu, Q., Kulhanek, D.K., Wang, J., 2014. Ages and magnetic structures of the South China Sea constrained by deep tow magnetic surveys and IODP Expedition 349. Geochem. Geophys. Geosyst. 15, 4958–4983.

Ma, W., Tian, J., Li, Q., Wang, P., 2011. Simulation of long eccentricity (400-kyr) cycle in ocean carbon reservoir during Miocene Climate optimum: weathering and nutrient response to orbital change. Geophys. Res. Lett. 38.

Martin, E.E., Scher, H.D., 2004. Preservation of seawater Sr and Nd isotopes in fossil fish teeth: bad news and good news. Earth Planet. Sci. Lett. 220, 25–39.

Menviel, L., Yu, J., Joos, F., Mouchet, A., Meissner, K.J., England, M.H., 2017. Poorly ventilated deep ocean at the Last Glacial Maximum inferred from carbon isotopes: a data-model comparison study. Paleoceanography 32, 2–17.

Peterson, C.D., Lisiecki, L.E., Stern, J.V., 2014. Deglacial whole-ocean $\delta^{13}C$ change estimated from 480 benthic foraminiferal records. Paleoceanography 29, 549–563.

Pisias, N.G., Shackleton, N., Hall, M., 1985. Stable isotope and calcium carbonate records from hydraulic piston cored Hole 574A: high-resolution records from the middle Miocene. In: Mayer, L., Theyer, F., Thomas, E., et al. (Eds.), Init. Rep. DSDP 85, pp. 735–748.

Qu, T., Girton, J.B., Whitehead, J.A., 2006. Deepwater overflow through Luzon Strait. J. Geophys. Res. 111.

Queano, K.L., Ali, J.R., Milsom, J., Aitchison, J.C., Pubellier, M., 2007. North Luzon and the Philippine Sea Plate motion model: insights following paleomagnetic, structural, and age-dating investigations. J. Geophys. Res., Solid Earth 112.

Raymo, M.E., Ruddiman, W.F., 1992. Tectonic forcing of late Cenozoic climate. Nature 359, 117–122.

Scher, H.D., Whittaker, J.M., Williams, S.E., Latimer, J.C., Kordesch, W.E., Delaney, M.L., 2015. Onset of Antarctic Circumpolar Current 30 million years ago as Tasmanian Gateway aligned with westerlies. Nature 523, 580–583.

Sclater, J.G., Meinke, L., Bennett, A., Murphy, C., 1985. The depth of the ocean through the Neogene. In: Kennett, J.P. (Ed.), The Miocene Ocean: Paleoceanography and Biogeography. The Geological Society of America, Boulder, CO, pp. 1–21.

Seton, M., Müller, R., Zahirovic, S., Gaina, C., Torsvik, T., Shephard, G., Talsma, A., Gurnis, M., Turner, M., Maus, S., 2012. Global continental and ocean basin reconstructions since 200 Ma. Earth-Sci. Rev. 113, 212–270.

Shevenell, A., Kennett, J., 2004. Paleoceanographic change during the middle Miocene climate revolution: an Antarctic stable isotope perspective. The Cenozoic Southern Ocean: Tectonics. In: Sedimentation, and Climate Change Between Australia and Antarctica, pp. 235–251.

Shevenell, A.E., Kennett, J.P., Lea, D.W., 2004. Middle Miocene Southern Ocean cooling and Antarctic cryosphere expansion. Science 305, 1766–1770.

Shevenell, A.E., Kennett, J.P., Lea, D.W., 2008. Middle Miocene ice sheet dynamics, deep-sea temperatures, and carbon cycling: a Southern Ocean perspective. Geochem. Geophys. Geosyst. 9.

Sigman, D.M., Hain, M.P., Haug, G.H., 2010. The polar ocean and glacial cycles in atmospheric CO_2 concentration. Nature 466, 47–55.

Skinner, L., McCave, I.N., Carter, L., Fallon, S., Scrivner, A.E., Primeau, F., 2015. Reduced ventilation and enhanced magnitude of the deep Pacific carbon pool during the last glacial period. Earth Planet. Sci. Lett. 411, 45–52.

Talley, L.D.P., Emery, G.L., Swift, W.J., Talley, J.H.L.D., 2011. Descriptive Physical Oceanography.

Taylor, B., Hayes, D.E., 1980. The Tectonic Evolution of the South China Basin. Geophys. Monogr., vol. 23, pp. 89–104.

Taylor, B., Hayes, D.E., 1983. Origin and history of the South China Sea basin. In: The Tectonic and Geologic Evolution of Southeast Asian Seas and Islands: Part 2, pp. 23–56.

Tian, J., Zhao, Q., Wang, P., Li, Q., Cheng, X., 2008. Astronomically modulated Neogene sediment records from the South China Sea. Paleoceanography 23.

Tian, J., Ma, W., Lyle, M.W., Shackford, J.K., 2014. Synchronous mid-Miocene upper and deep oceanic $\delta^{13}C$ changes in the east equatorial Pacific linked to ocean cooling and ice sheet expansion. Earth Planet. Sci. Lett. 406, 72–80.

Tian, J., Shevenell, A., Wang, P., Zhao, Q., Li, Q., Cheng, X., 2009. Reorganization of Pacific Deep Waters linked to middle Miocene Antarctic cryosphere expansion: a perspective from the South China Sea. Palaeogeogr. Palaeoclimatol. Palaeoecol. 284, 375–382.

Tian, J., Yang, M., Lyle, M.W., Wilkens, R., Shackford, J.K., 2013. Obliquity and long eccentricity pacing of the Middle Miocene climate transition. Geochem. Geophys. Geosyst. 14, 1740–1755.

Toggweiler, J., Russell, J.L., Carson, S., 2006. Midlatitude westerlies, atmospheric CO_2, and climate change during the ice ages. Paleoceanography 21.

Vincent, E., Berger, W.H., 1985. Carbon dioxide and polar cooling in the Miocene: the Monterey hypothesis. In: The Carbon Cycle and Atmospheric CO: Natural Variations Archean to Present, pp. 455–468.

Wang, L.-W., Lin, H.-L., 2004. Data report: carbonate and organic carbon contents of sediments from Sites 1143 and 1146 in the South China Sea. In: Proceedings of the Ocean Drilling Program, Scientific Results, pp. 1–9.

Wang, P., Blum, P., Nessler, S., 2000. Proceedings of the Ocean Drilling Program. Texas A & M University.

Wang, R., Li, J., Li, B., 2004. 21. Data Report: Late Miocene–Quaternary Biogenic Opal Accumulation at ODP Site 1143. Southern South China Sea.

Woodruff, F., Savin, S., 1991. Mid-Miocene isotope stratigraphy in the deep sea: high-resolution correlations, paleoclimatic cycles, and sediment preservation. Paleoceanography 6, 755–806.

Wu, Q., Colin, C., Liu, Z., Bassinot, F., Dubois-Dauphin, Q., Douville, E., Thil, F., Siani, G., 2017. Foraminiferal εNd in the deep north-western subtropical Pacific Ocean: tracing changes in weathering input over the last 30,000 years. Chem. Geol. 470, 55–66.

Yu, J., Anderson, R.F., Jin, Z., Rae, J.W., Opdyke, B.N., Eggins, S.M., 2013. Responses of the deep ocean carbonate system to carbon reorganization during the Last Glacial–interglacial cycle. Quat. Sci. Rev. 76, 39–52.

Yu, J., Anderson, R.F., Rohling, E.J., 2014. Deep Ocean carbonate chemistry and glacial–interglacial atmospheric CO_2 changes. Oceanography 27, 16–25.

Yu, J., Elderfield, H., Hönisch, B., 2007. B/Ca in planktonic foraminifera as a proxy for surface seawater pH. Paleoceanography 22.

Yu, J., Menviel, L., Jin, Z.D., Thornalley, D.J.R., Barker, S., Marino, G., Rohling, E.J., Cai, Y., Zhang, F., Wang, X., Dai, Y., Chen, P., Broecker, W.S., 2016. Sequestration of carbon in the deep Atlantic during the last glaciation. Nat. Geosci. 9, 319–324.